ACS OMEGA

http://pubs.acs.org/journal/acsodf

Article

Design and Development of High-Entropy Alloys with a Tailored Composition and Phase Structure Based on Thermodynamic Parameters and Film Thickness Using a Novel Combinatorial Target

Khurshed Alam,[⊥] Woohyung Jang,[⊥] Geonwoo Jeong, Chul-Kyu Park,* Kwangmin Lee,* and Hoonsung Cho*

Cite This: *ACS Omega* 2023, 8, 28333−28343

Read Online

ACCESS | Metrics & More | Article Recommendations | Supporting Information

ABSTRACT: This study presents a novel synthesis route for high-entropy alloys (HEAs) and high-entropy metallic glass (HEMG) using radio frequency (RF) magnetron sputtering and controlling the HEA phase selection according to atomic size difference (δ) and film thickness. The preparation of HEAs using sputtering requires either multitargets or the preparation of a target containing at least five distinct elements. In developing HEA-preparation techniques, the emergence of a novel sputtering target system is promising to prepare a wide range of HEAs. A new HEA-preparation technique is developed to avoid multitargets and configure the target elements with the required components in a single target system. Because of a customizable target facility, initially, a TiZrNbMoTaCr target emerged with an amorphous phase owing to a high δ value of 7.6, which was followed by a solid solution (SS) by lowering the δ value to 5 ($\leq$6.6). Thus, this system was tested for the first time to prepare TiZrNbMoTa HEA and TiZrNbMoTa HEMG via RF magnetron sputtering. Both films were analyzed using X-ray diffraction (XRD), X-ray photoelectron spectroscopy, field emission scanning electron microscopy cross-sectional thickness, and atomic force microscopy (AFM). Furthermore, HEMG showed higher hardness 10.3 ($\pm$0.17) GPa, modulus 186 ($\pm$7) GPa, elastic deformation (0.055) and plastic deformation (0.032 GPa), smooth surface, lower corrosion current density (I_{corr}), and robust cell viability compared to CP-Ti and HEA. XRD analysis of the film showed SS with a body-centered cubic (BCC) structure with (110) as the preferred orientation. The valence electron concentration [VEC = 4.8 (<6.87)] also confirmed the BCC structure. Furthermore, the morphology of the thin film was analyzed through AFM, revealing a smooth surface for HEMG. Inclusively, the concept of configurational entropy (ΔS_{mix}) is applied and the crystalline phase is achieved at room temperature, optimizing the processing by avoiding further furnace usage.

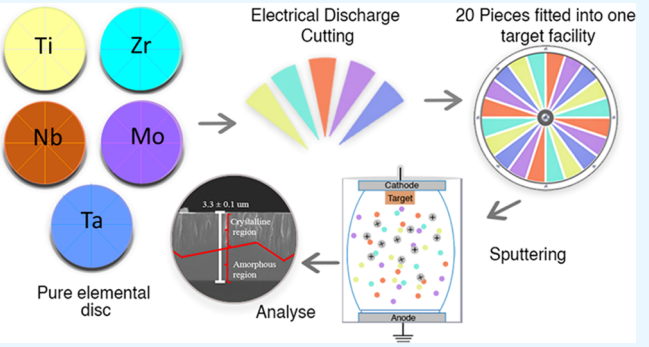

1. INTRODUCTION

High-entropy alloys (HEAs) have attracted significant interest and emerged as a new research area since they were first reported in 2004 by Cantor et al. and Yeh et al.[1−3] HEAs have at least five elements, each with a similar accommodating probability in a crystal lattice site.[4] The existence of numerous mixing elements in HEAs favors a high configurational entropy.[5,6] Surprisingly, even with this novel concept in alloy development, researchers have managed to produce only solid solutions (SS) of various HEAs prepared thus far. Moreover, after the commercial use of alloys, the most advanced type of alloy development has become a subject of debate regarding overcoming the limitations of conventional alloys (CAs) that can be used in a wide range of applications, e.g., biomedical and energy sector, and making them environment friendly.[6] Some prominent features distinguishing HEAs from CAs in a wide temperature range include sluggish diffusion, lattice distortion, high mixing entropy, and cocktail effect.[4] A combination of these effects affects the corrosion, tribocorrosion, strength, hardness, ductility, oxidation/wear, and erosion resistance of the alloys.[4]

The study of HEAs has significantly advanced during the last decade, producing numerous research papers and using various techniques for developing HEAs with optimum properties, e.g., powder metallurgy, laser cladding, spraying, casting, and electrochemical and electrospark deposition.[4] However, it is still important to consider the results of various manufacturing processes because the properties of HEAs are highly

Received: April 3, 2023
Accepted: July 12, 2023
Published: July 26, 2023

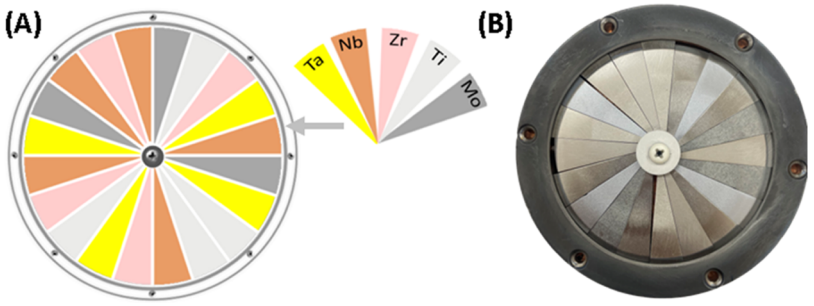

Figure 1. (a) Schematic representation of RF/DC magnetron sputtering target setup and (b) digital photograph of the target.

dependent on the processing route.[7] Most of these techniques require high temperatures, material usage, cost, and processing time and cause inhomogeneity.[7] However, thin film synthesis through RF magnetron sputtering can be considered a feasible method for realizing coating on various substrates and applications in extremely harsh environments such as radiations, the aerospace industry, and cutting instruments.[4] Researchers from the materials science community have struggled to develop bioengineered alloys that can bridge the gap of the limitations caused by some of the prominent bio-implants, which cause severe allergic and adverse effects, causing ultimate failure and inflammations.[8−10] The developed HEAs have shown promising applications as biomaterials and have surpassed the limitations of bioengineered materials.[11] Some of the most widely used bioengineered alloys that have not been completely successful are 316 L stainless steel, CoCr alloys, commercially pure titanium (CP-Ti), Ti-6Al-4V, and NiTi.[11]

Researchers have investigated the preparation of HEAs owing to the use of HEAs in a wide temperature range and limited research on the synthesis of HEAs for prospective applications.[4] HEAs are considered to have excellent mechanical properties under high-temperature usage, representing a new class of materials with unique properties.[12] Further, researchers have discovered several applications of HEAs in harsh environments, such as coating on cutting tools, resistance to radiation, aerospace industry, wear resistance, and biomedical implants.[4] Thus, HEA synthesis is crucial for a wide range of applications and to overcome the limitations of CAs. Various thermodynamic parameters, e.g., δ, electronegativity, valence electron concentration (VEC), mixing entropy (ΔS_{mix}), and mixing enthalpy (ΔH_{mix}), are rationalized statistically for the synthesis of SSs or amorphous phase in HEAs.[13,14] The most critical parameters in synthesizing SSs are δ, ΔH_{mix}, and ΔS_{mix}.[13,15] Moreover, is it possible to design and predict the HEA phase as an SS or amorphous phase? Yes, if $\delta \leq 6.6$, -11.6 kJ/mol $< \Delta H_{mix} <$ 3.2 kJ/mol, and $12 \leq \Delta S_{mix} \leq 17.5$ (J/K·mol) (or $\Delta S_{mix} \geq 1.61$R).

Herein, we report the development of a novel method specialized for HEAs in a single target to avoid multitargets and configure the target elements with the required components, thereby avoiding target preparation, high equipment usage, and high processing time. Surprisingly, crystalline-phase TiZrNbMoTa (HEA) is obtained at room temperature (RT), and the phase structure is controlled by tailoring δ, ΔH_{mix}, ΔS_{mix}, and film thickness. The surprising achievement of this study is that crystallinity at RT is obtained and is attributed to the sluggish diffusion caused by the high configurational entropy (ΔS_{mix}) effect in HEAs. Thus, the SS obtained is metastable, stable at high temperatures, and frozen at RT, similar to the amorphous phase obtained at a rapid cooling rate.[14] This phenomenon makes the high-entropy effect a factor involved in creating SS phases in HEAs at RT.[14] Furthermore, crystallinity control with film thickness is attributable to the high-quenching rate of magnetron sputtering (>106 K/s) for sputtered atoms during film synthesis.[12] This high-quenching-rate phenomenon leads to the synthesis of an amorphous phase (HEMG) with a low film thickness (833 nm) deposited for 30 min.[12] However, the coating thickness for the crystalline region is 3.3 μm, deposited over a period of 2 h, providing enough time for growth as a well-defined crystalline phase. The δ parameter for TiZrNbMoTa is brought in the SS range, i.e., $\delta = 5$ ($\leq$6.6) from 7.6 in the case of TiZrNbMoTaCr. By using the prominent thermodynamic parameters δ, ΔH_{mix}, and ΔS_{mix}, a validation criterion for preparing SS of HEAs and the selection of elements with high biocompatibility, i.e., Ti, Zr, Nb, Mo, and Ta for orthopedic implants are preferred. Thus, TiZrNbMoTa HEA and HEMG were coated on a CP-Ti substrate as the main composition to modify its surface properties for biological applications. The cell viability, corrosion analysis, hardness, and modulus were considerably improved for the HEMG.

2. EXPERIMENTAL SECTION

2.1. Target Preparation. The target materials were procured individually from Thifine Korea and cut into pieces by electrical discharge machining with an angle of 18°, configurating 20 pieces at a time. The target pieces shown in (Figure 1a) were configured in a single target system with a ceramic screw. Thus, a new target system capable of tailoring the composition for desired HEAs for a wide range of applications was developed. In addition, the position of each element and the number of elements are important for maintaining a constant alloy composition. The target materials were polished with emery paper and configured. A fast sputtering process and reproducible sputtering target are required to replace or change the target composition for prospective applications.

2.2. Thin Film Coating. All of the coatings were prepared using RF magnetron sputtering. An argon atmosphere was provided to sputter the target elements for thin film growth on the substrate. Silicon wafer substrates were used for X-ray photoelectron spectroscopy (XPS), X-ray diffraction (XRD), field emission scanning electron microscopy (FE-SEM) cross-sectional analysis, energy-dispersive X-ray spectroscopy (EDS), and nanoindentation characterizations. A CP-Ti substrate was provided for the evaluation of cell viability (MC3T3-E1 osteoblast cells) and corrosion analysis. Ti samples were well cleaned by polishing with emery paper of grit size 400−1200

https://doi.org/10.1021/acsomega.3c02222
ACS Omega 2023, 8, 28333−28343

and ultrasonically for 5 min each in ethanol and distilled water. The target elements were pre-sputtered for 10 min to remove adherent contaminants, and then the samples were loaded using a load lock chamber. The process was performed for 2 h for HEA and 30 min for HEMG with a substrate rotation of 10 rpm at RT. The parameters used are given in Table 1.

Table 1. Parameters Used for the Synthesis of Thin Films

deposition temp	room temperature (RT)
base pressure	2.4×10^{-5} torr
argon gas	30 sccm
pre-sputtering	10 mTorr
working pressure	5 mTorr (C)
RF power	200 W
rotation	10 rpm
deposition time	120 min (HEA), 30 min (HEMG)
deposition rate	27.5 nm/min

2.3. Thin Film Characterization. XRD measurement (with Cu Kα radiation) was performed to analyze the crystallinity and phase structure of the prepared films. The scan rate was kept low (1°/min) for better resolution. The step size, omega, and 2θ range were 0.02, 1.5, and 10−90°, respectively. Further, the operating voltage was 45 kV. The thin films' thickness measurement and EDS analysis were performed using FE-SEM (model: Gemini 500). EDS (Oxford) was employed to evaluate the homogeneity of the deposited thin films, and surface chemistry and oxidation states before and after the argon etching were analyzed by XPS (model: K-α +) using an Al Kα X-ray analyzer. AFM analyses were performed in an ambient environment using the NX20 atomic force microscope with the noncontact mode for surface morphology. A piezo scanner (size: 100 × 100 × 15 μm^3) was used for the fine movement. A maximum load of 3 mN was applied for nanoindentation measurements using a nano-indenter (Type: Berkovich, serial number: BBB-39, material: Diamond). Both hardness and modulus values were calculated using loading and unloading conditions. Corrosion analysis was conducted using the VSP-300 potentiostat/galvanostat model number KKR-21738740-40000018 in a K0235 flat cell type with a maximum volume of 250 mL. EC-Lab V11.33 version was used to analyze the corrosion results. A coating film was used as the working electrode (exposed area = 1 cm^2), a platinum mesh was used as a counter electrode, and Ag/AgCl (saturated KCl filling solution) was used as a reference electrode. Argon gas was supplied constantly to prevent ions from settling in aqueous Ringer's physiological solution. The electrolytes used were NaCl (9 g/L), $CaCl_2$ (0.24 g/L), KCl (0.43 g/L), and $NaHCO_3$ (0.23 g/L).

2.4. Biocompatibility Assay. MC3T3 osteoblast cells were used for testing cell viability. Seeding was performed at a density of 5 × 10^4 cells/well (25% confluency) using 24-well plates in 1 mL α MEM media (LM008-53) for MC3T3 cells. The cells were allowed to attach to the bottom for three days at 37 °C under a 5% CO_2 environment. After three days of

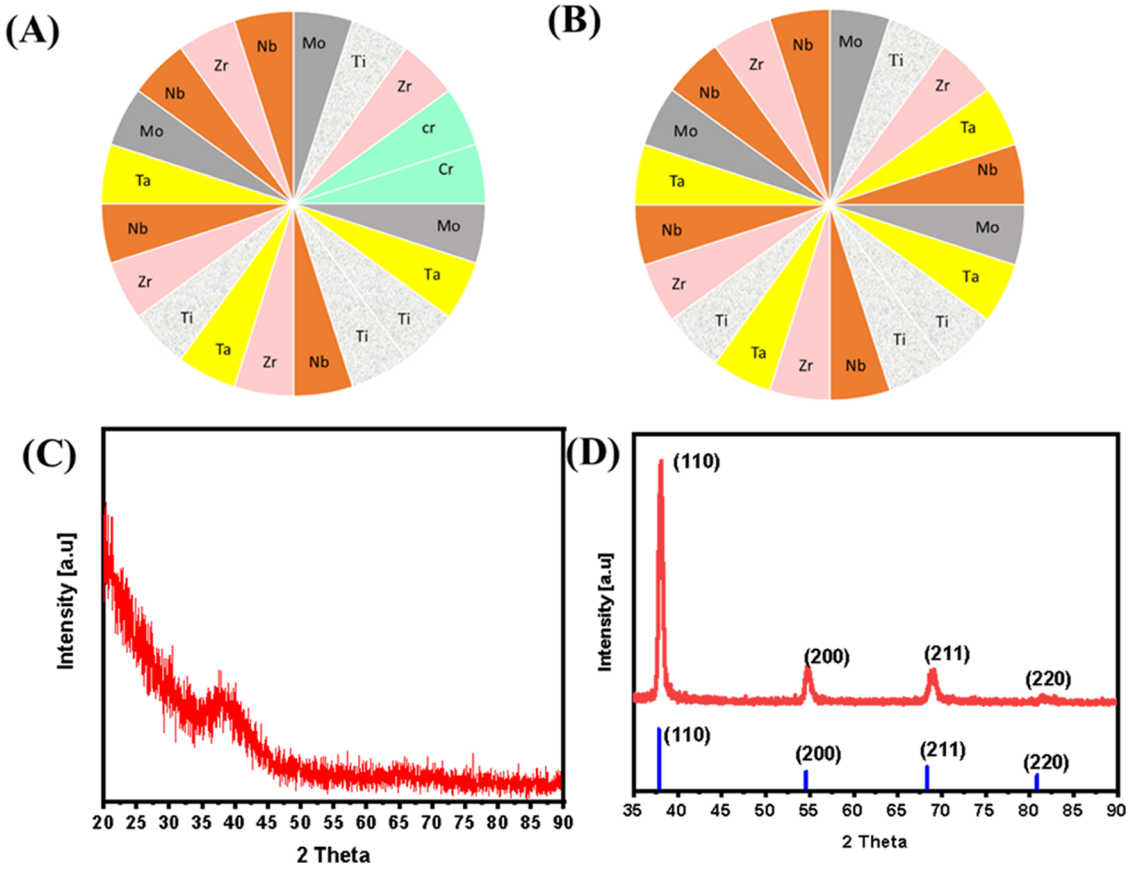

Figure 2. Controlling the phase structure by tailoring δ at room temperature (RT): (a) configuration of target elements of TiZrNbMoTaCr, (b) configuration of target elements of TiZrNbMoTa, (c) amorphous structure obtained for TiZrNbMoTaCr [δ = 7.46 (≥6.6)], and (d) Crystalline structure obtained for TiZrNbMoTa by the removal of Cr [δ = 5.1 (≤6.6)] after 120 min of deposition.

https://doi.org/10.1021/acsomega.3c02222
ACS Omega 2023, 8, 28333−28343

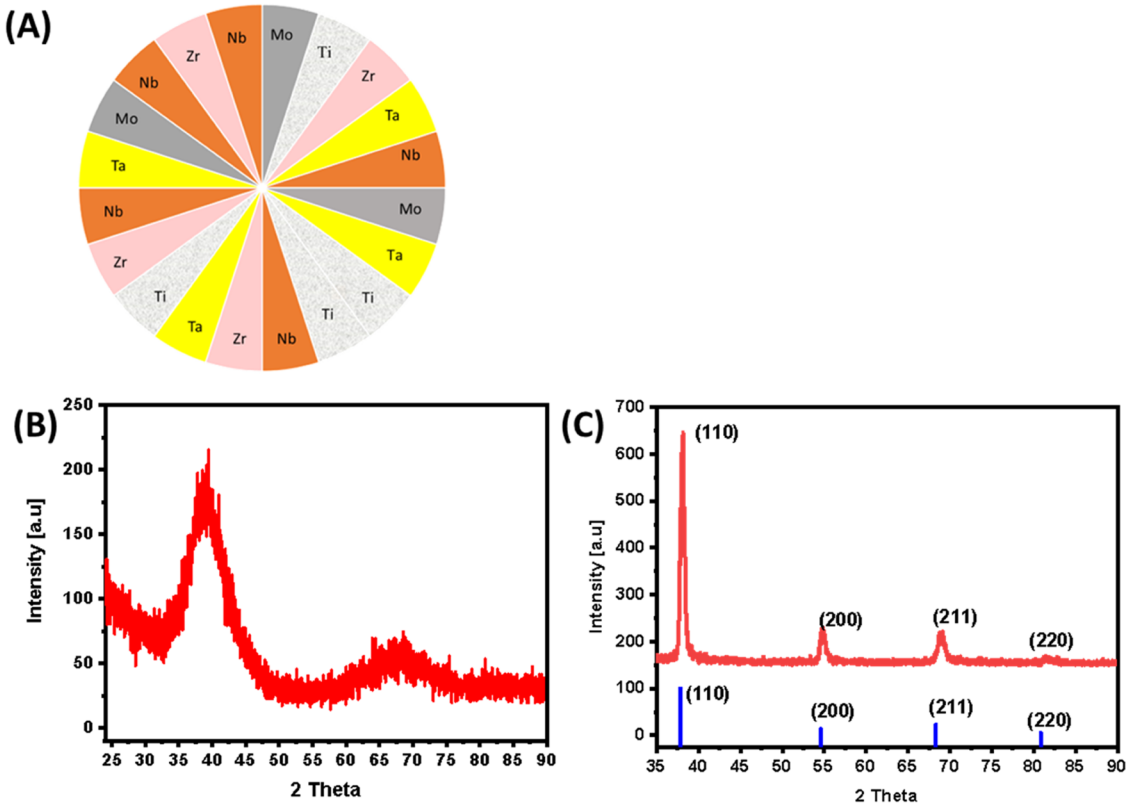

Figure 3. Controlling the phase structure with film thickness: (a) target element combination, (b) amorphous phase with a film thickness of 833 nm after 30 min of deposition, and (c) solid solution phase with a film thickness of 3.3 μm after 120 min of deposition, analyzed using X'Pert HighScore Plus software.

incubation, the media was removed and washed with 1× phosphate-buffered saline (PBS) twice, followed by 0.1 mg/mL MTT (3-(4,5-dimethylthiazol2-yl)-2, 5-diphenyltetrazolium bromide) with the addition of 540-μL α-MEM growth media and 60 μL MTT assay in each well (10% MTT assay). After two hours in the incubator, the media was replaced with 600 μL of MTT solvent dimethylsulfoxide (DMSO). The absorbance was taken at 570 nm using the Varioskan LUX reader to evaluate cell viability.

3. RESULTS AND DISCUSSION

A single target system was designed to reduce preparation time and optimize costs, as illustrated in Figure 1. It was configured using HEAs (TiZrNbMoTaCr or TiZrNbMoTa). The target could comprise a maximum of 20 pieces, which could be used as an advantage for tailoring the composition. The purity of each ingredient was always 99.9%.

Table 2. Crystallite Size Measured Using XRD Data for HEA and HEMG

	TiZrNbMoTa (HEA)	TiZrNbMoTa (HEMG)
2θ	crystallite size (nm)	crystallite size (nm)
38.13	0.28	0.04
54.79	0.22	
69.11	0.19	
81.47	1.97	

The XRD analysis for the TiZrNbMoTaCr HEA thin film on the silicon substrate is presented in Figure 2. The enthalpy of mixing, ΔH_{mix}, calculated for both targets was −6 and −1.3, which was in the range $-11.6 \leq \Delta H_{mix} \leq 3.2$ kJ/mol, a validation criterion for preparing the SS.[16] The range for atomic size difference is $\delta \leq 6.6$, an additional compulsory parameter to achieve a crystalline structure.[17−19] ΔH_{mix}, δ, and other parameters can be calculated using the following equations, and the corresponding calculated values are given in Table 4.

$$\Delta H_{mix} = \sum_{i=1, i\neq j}^{n} (4\Delta H_{mix} AB) \quad (1)$$

$$\delta = \sqrt[100]{\sum_{i=1}^{r} C_i(1 - r_{i/\overline{r}})\,2} \quad (2)$$

where $\overline{r} = \sum_{i=1}^{n} ciri$.

$$VEC = \sum_{i=1}^{N} C_i(VEC)_i \quad (3)$$

$$\Delta S_{mix} = -R \sum_{1=1}^{N} C_1 \ln c_i \quad (4)$$

$$\Omega = \frac{T_m \Delta S_{mix}}{\Delta H_{mix}} \quad (5)$$

where $T_m = \sum_{i=1}^{N} C_i\,(Tm)_i$

C_i belongs to the atomic percentages, and $(VEC)_i$ is the valance electron concentration of ith element, R = 8.314 J/K·mol is the universal gas constant. ΔH_{mixAB} is the enthalpy of mixing for binary elements given in Table S4.

https://doi.org/10.1021/acsomega.3c02222
ACS Omega 2023, 8, 28333−28343

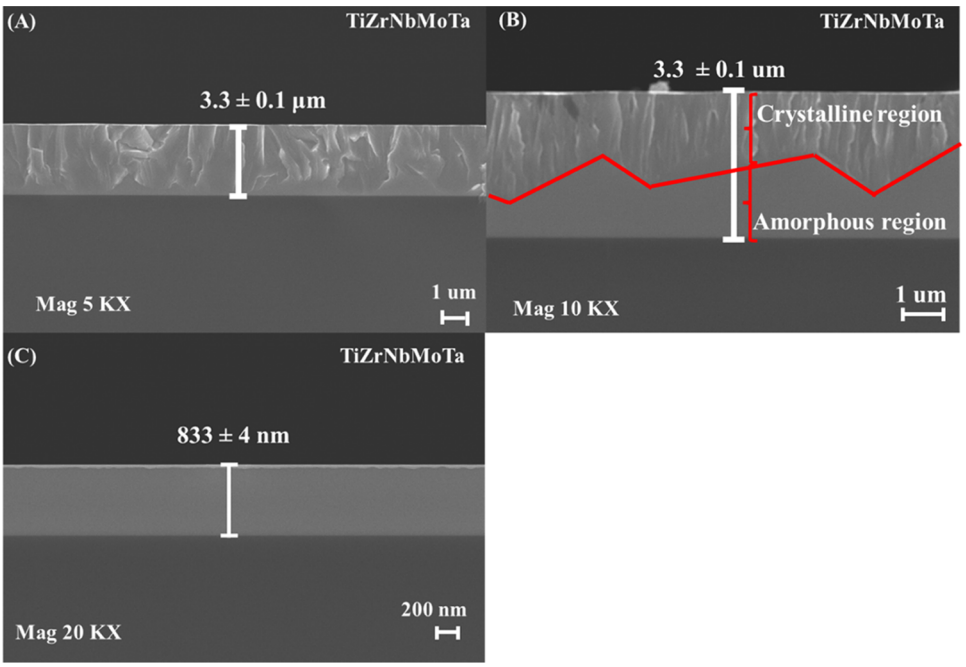

Figure 4. Thin Film coating of (a) HEA with 120-min deposition, (b) HEA highlighting different phase regions at a higher magnification after 120 min deposition, and (c) HEMG after 30 min deposition.

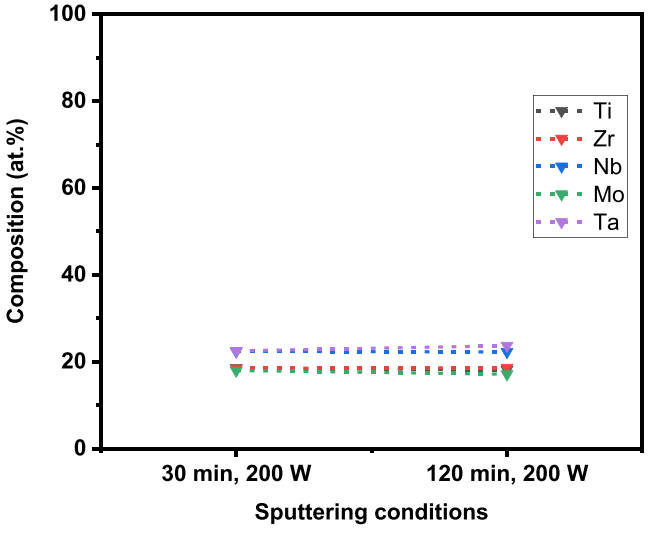

Figure 5. Chemical composition of TiZrNbMoTa HEA and HEMG deposited with different coatings evaluated through EDS analysis.

Table 3. Similar Compositions for TiZrNbMoTa HEA and HEMG

elements	atom % (HEA)	atom % (HEMG)
Ti	18.2	18.6
Zr	18.7	18.5
Nb	22.3	22.4
Mo	17.2	18
Ta	23.8	22.5

The atomic size difference is reduced and brought within the crystalline region, i.e., $\delta \leq 6.6$. Reduction of δ to bring it within the SS range is achieved by removing Cr from the target composition. The SS range cannot be controlled by a single mixing entropy factor and enthalpy of mixing.[13] Rather, it is statistically defined that the SS phase can be controlled by controlling three main factors simultaneously: ΔH_{mix}, ΔS_{mix}, and δ.[13] Furthermore, the most dominating factor for developing a SS is δ, which has been considered the most critical parameter.[13] Removing Cr is not the criterion involved in controlling the SS phase. One can use Cr, but the combination of elements should satisfy ΔH_{mix}, ΔS_{mix}, and δ simultaneously for the SS phase.[13] Thus, our target system enables reconsideration of the target combination of TiZrNbMoTa, where the values for ΔH_{mix}, ΔS_{mix}, and δ are satisfied simultaneously in creating the SS phase, as revealed by Table 4 and Figure 2d. The XRD analysis of TiZrNbMoTa (HEA) after the removal of Cr revealed a well-defined crystalline, as shown in (Figure 2d). A film thickness of 3.3 μm was obtained in a deposition period of 120 min. Various peaks appeared at 38.1, 54.7, 69, and 81.6° corresponding to (110), (200), (211), and (220), respectively, upon analysis with X'Pert HighScore Plus, conforming to the BCC phase. However, a complete amorphous structure is obtained with a target configuration of TiZrNbMoTaCr due to δ = 7.46, ≥6.6 as shown in Figure 2c. Furthermore, the similar target configuration of TiZrNbMoTa crystallinity is controlled by low film thickness, as shown in (Figure 3b), forming an amorphous phase (HEMG) with a film thickness of 833 nm and a crystalline phase (HEA) with a film thickness of 3.3 μm. The crystallite size measured using the Scherrer equation for both TiZrNbMoTa HEA and HEMG is

$$L = \frac{k\lambda}{\beta \cos \theta} \tag{6}$$

where L is the grain size, k is the shape factor (0.89), λ is the wavelength (Cu kα = 0.154 nm), θ is the diffraction angle, and β is the full width at half-maximum obtained from XRD data. The crystallite size thus obtained for an SS and amorphous TiZrNbMoTa is given in Table 2.

The lattice parameter calculated for each plane, using the following equations, was 3.3 Å.[20]

https://doi.org/10.1021/acsomega.3c02222
ACS Omega 2023, 8, 28333−28343

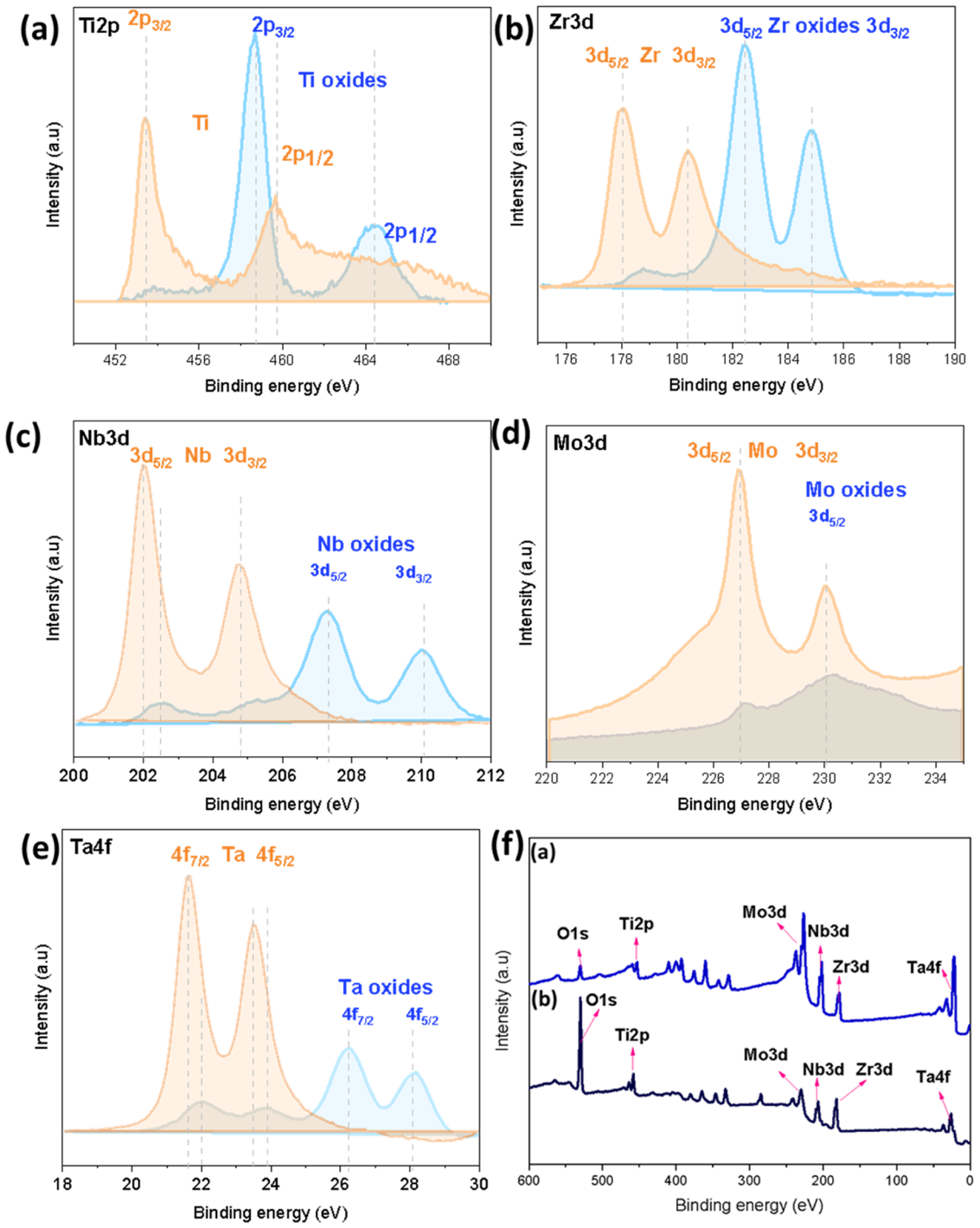

Figure 6. Detailed analysis of the oxidation of TiZrNbMoTa HEMG after merging the peaks before (blue) and after Ar^+ etching (orange) obtained through XPS analysis: (a) Ti 2p, (b) Zr 3d (c) Nb 3d, (d) Mo 3d, (e) Ta 4f, (f) f(a) XPS survey spectra after Ar^+ etching, and f(b) before Ar^+ etching.

$$a = d\sqrt{h^2 + k^2 + l^2} \tag{7}$$

where d is calculated by

$$\lambda = 2d \sin\theta \tag{8}$$

The cross-sectional thickness of the thin film coatings is shown in Figure 4. The thickness for the crystalline region prepared with 120 min of deposition was 3.3 μm, and the amorphous structure controlled with the film thickness had a film thickness of 833 nm after 30 min of deposition, as shown in Figure 4a,c. Both films were grown with a constant deposition rate of 27.5 nm/min under the same sputtering conditions. Figure 4b, which shows a high-magnification image, reveals that initially, the film grows as amorphous and then starts growing in the crystalline region. Figure 5 compares the chemical composition obtained with different coatings, analyzed through EDS, showing similar compositions. In addition, all the elements were found to be homogeneously distributed, as confirmed by EDS-layered cross-sectional imaging, as shown in Figure S1. The composition is summarized in Table 3. Furthermore, the morphology of the

https://doi.org/10.1021/acsomega.3c02222
ACS Omega 2023, 8, 28333−28343

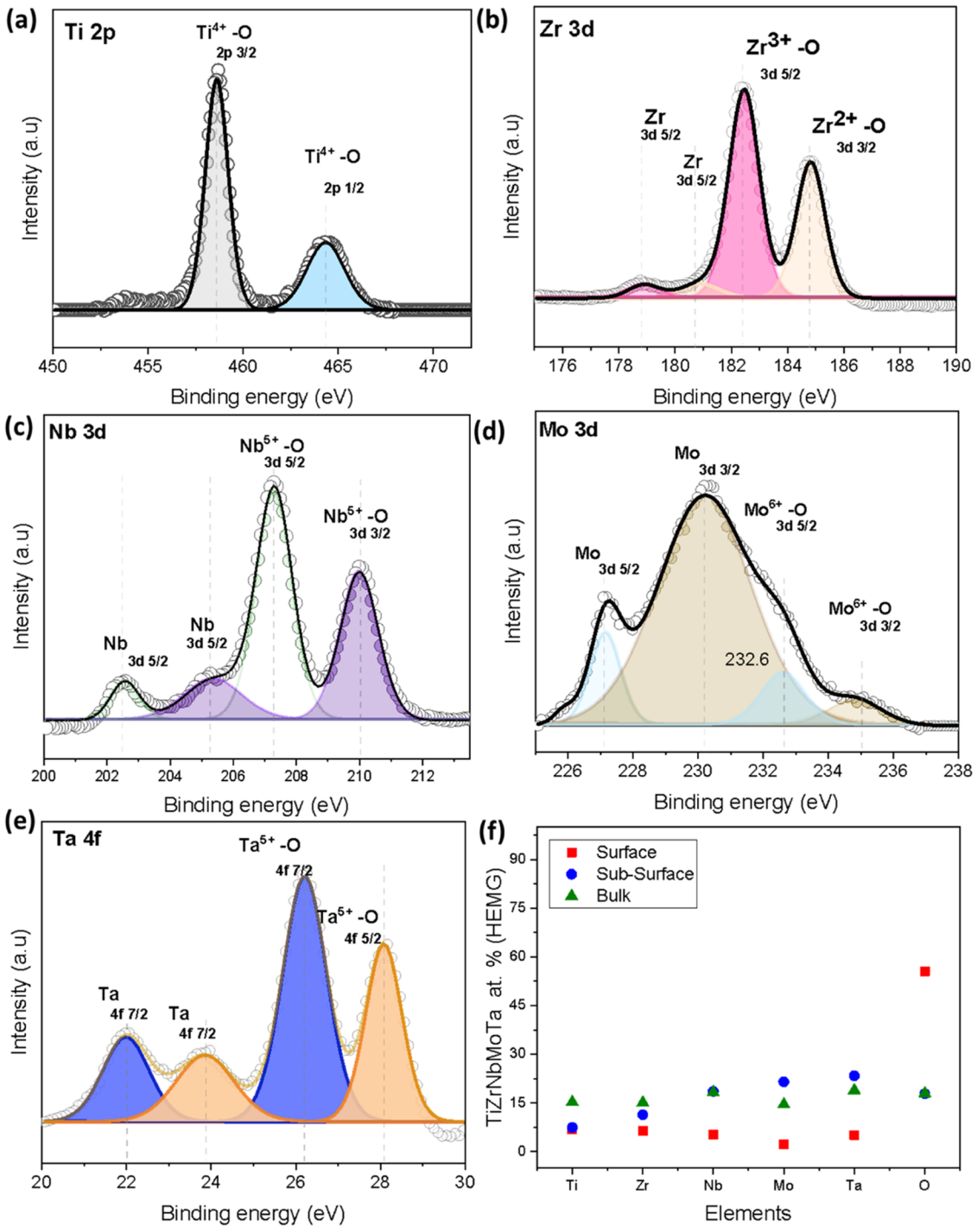

Figure 7. Binding energy obtained through the XPS analysis of TiZrNbMoTa HEMG to analyze the chemical bonding state of the sample surface: (a) Ti 2p, (b) Zr 3d, (c) Nb 3d, (d) Mo 3d, (e) Ta 4f, and (f) comparison of relative atomic compositions at different surface levels (surface, sub-surface, and bulk EDS).

thin film was analyzed through AFM to determine the surface roughness, revealing a porous structure for HEA and a smoother surface for HEMG, as shown in Figure 8. R_q (root-mean-square roughness) = 9.2 and R_a (average roughness) = 5.4, indicating that a structure with higher roughness and highly porous was obtained. At the same time, HEMG had no porosity and was smoother, with R_q = 3.7 and R_a = 2.88, showing considerably lower roughness compared to HEA.

The CP-Ti surface modified with coatings of different phase structures showed different cell viabilities and corrosion-related properties; in particular, HEMG showed considerably better cell proliferation. Similar significant cell viability for TiZrNbMoTa alloy was observed for osteoblasts and stem cells.[22] This highly biocompatible nature of TiZrNbMoTa HEMG is attributed to the stable oxide-layer formation, which further reduces the chances of further corrosion owing to its natural passivation.[22] Accordingly, a detailed surface analysis was performed by XPS to study the functional groups of TiZrNbMoTa. Furthermore, XPS analysis was limited to the surface with a probing depth up to 10 nm.[23] Meanwhile, the

https://doi.org/10.1021/acsomega.3c02222
ACS Omega 2023, 8, 28333−28343

Table 4. Parameters for Designing the Solid Solution[16,21]

parameters	literature values	experimental values (RHEA)
ΔS_{mix}	$12 \leq \Delta S_{mix} \geq 17.5$ (J/K·mol)	1.6R = 13.315 J/K·mol
ΔH_{mix}	$-11.6 < \Delta H_{mix} < 3.2$ (kJ mol^{-1})	−1.306
Ω	≥1.1	26.9 (>1)
δ	≤6.6%	5.14
VEC	VEC ≥ 8.0 (FCC) VEC ≤ 6.87 (BCC) 6.87 <VEC <8.0 (BCC + FCC)	4.8 (<6.87) (BCC)

surfaces of the alloys have a tendency to form an oxide layer in an open environment.[24] Therefore, XPS analysis was performed to study the effect of etching with Ar plasma (Ar^+) for 20 min to expose the inner native coating surface. The XPS survey spectra and electron spectra at the core level were acquired, and the effect of Ar^+ plasma etching was extensively studied; overlapped peaks for before Ar^+ plasma etching (blue curves) and etching with Ar^+ (orange curves) were observed, as shown in Figure 6. The surface before Ar^+ plasma etching was found to be in a highly oxidized state, while the surface after Ar^+ plasma etching (sub-surface) showed a significant reduction in the O 1s peak and limited the C 1s peak appearance as shown in Figure 6fa. Furthermore, the metallic species intensity increased and became more evident with Ar^+ plasma etching. These results are consistent with ref.[4] The corresponding binding energies are listed in Table S1. The individual electron spectra at the core level before Ar^+ plasma etching were for the oxidized form.[25] However, the individual spectra were obtained at lower energy states after Ar^+ plasma etching (during XPS analysis), corresponding to pure metallic conditions.[26] As shown in Figure 6a,b, both Ti and Zr compositions were higher, which is also confirmed by Table S2. Further, the XPS survey spectra in Figure 6fa show a significant decrease in the O 1s peak compared to the sub-surface (before Ar^+ plasma etching). Thus, the high-intensity O1s peak before etching is attributed to transition metallic oxides, namely, Nb^{5+} (Nb_2O_5), Ta^{5+}(Ta_2O_5), Ti^{4+} (TiO2), Zr^{3+} (Zr_2O_3), Zr^{2+} (ZrO_2), and Mo^{6+} (MoO_3).[26−28] This high-intensity O1s peak is more clearly explained in Figure 7f, showing the relative atomic composition, where the surface has a higher percentage of oxygen (55.49%), 17.8 (sub-surface),

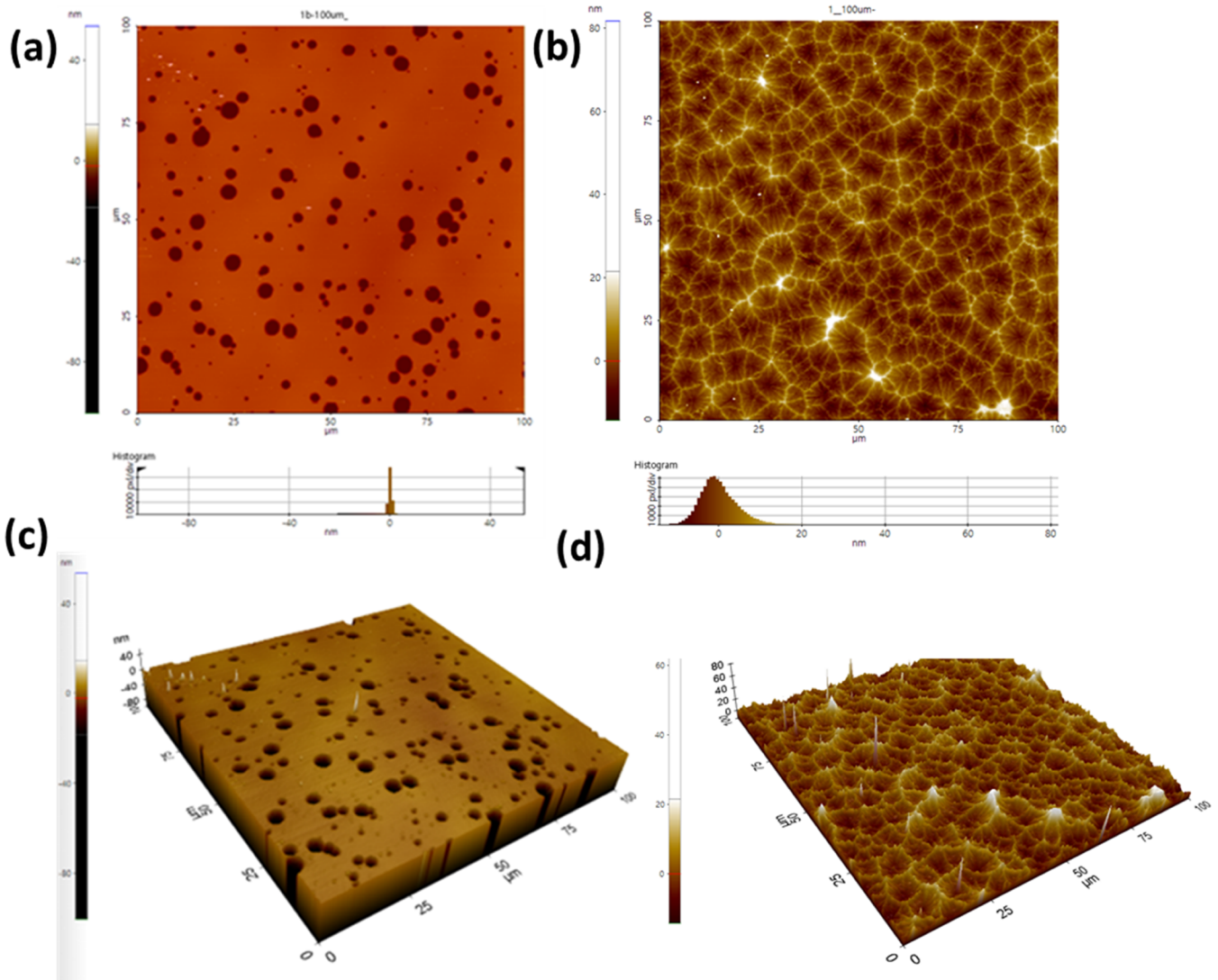

Figure 8. Surface morphology obtained by AFM: (a)TiZrNbMoTa HEA top surface analysis, (b) TiZrNbMoTa HEMG top surface analysis, (c) 3D topography analysis of TiZrNbMoTa HEA, and (d) 3D topography analysis of TiZrNbMoTa HEMG.

https://doi.org/10.1021/acsomega.3c02222
ACS Omega 2023, 8, 28333−28343

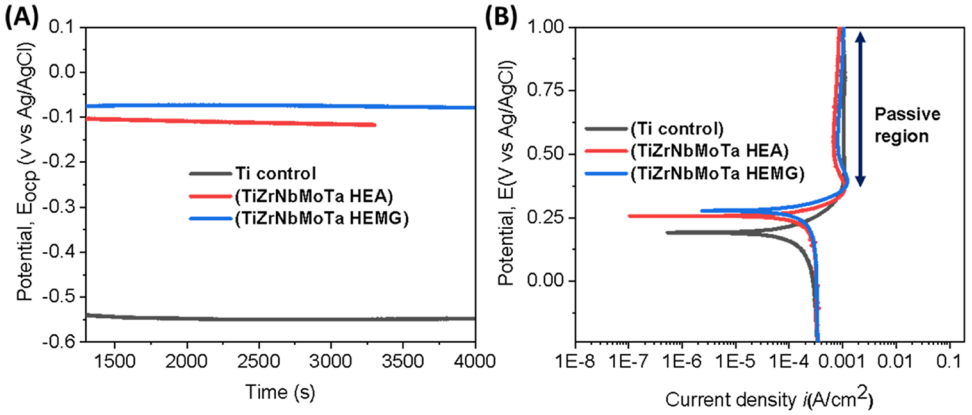

Figure 9. (a) Open-circuit potential (E_{oc}) for TiZrNbMoTa RHEA, RHEMG, and CP-Ti immersed in physiological Ringer's solution at RT prior to obtaining potentiodynamic curves and (b) potentiodynamic polarization curves of TiZrNbMoTa HEA (red), HEMG (blue), and CP-Ti (black) are included for comparison.

Table 5. Electrochemical Characterization in Ringer's Solution at RT for TiZrNbMoTa (RHEA and RHEMG) for Comparing the Corrosion Resistance

samples	E_{corr} (V)	I_{corr} (μA/cm^2)	βa (V)	βc (v)	CR (mmpy)
Ti (control)	0.19	0.15	0.177	0.612	1.23×10^{-3}
TiZrNbMoTa (HEA)	0.25	0.25	0.154	1.98	0.17
TiZrNbMoTa (HEMG)	0.28	0.22	0.13	1.3	0.15

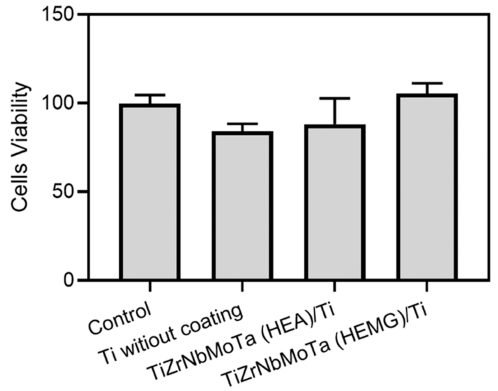

Figure 10. MTT assay analysis for A10 cell viability.

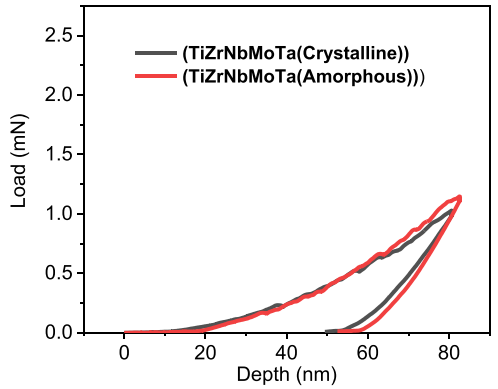

Figure 11. Nanoindentation plot with a 10% depth (80 nm) of load against penetration depth.

and 17.9 (bulk), as given in Table S2. The HEA and HEMG alloys were prepared with a similar and nearly equiatomic composition, as given in Table 3. Figure 7f further highlights that Ti and Zr have a higher composition on the surface, which decreases going deeper into the native film surface, indicating near equiatomic compositions in deep cross-sectional EDS analysis (Table 4).

The XPS survey spectra were further deconvoluted for every individual peak both for the as-deposited HEMG (Figure 7) and HEA (Figure S3). Figures 6 and 7 show different graphs: Figure 6 shows the detailed XPS analysis of the surface [before Ar^+ etching (blue curves)] and sub-surface analysis [after Ar^+ etching (orange curves)], and Figure 7 shows the chemical bonding state of the sample surface obtained through XPS analysis for individual elements. The bonding energies at the electron core level are listed in Table S1. A careful examination of the individual spectra of each element in both amorphous and crystalline phases revealed that the crystalline-phase individual spectra showed the oxidation state along with a robust peak for each individual pure metallic peak for Ti, Zr, Nb, Mo, and Ta, as shown in Figure S3. However, in the case of HEMG, no obvious peak was observed at the metallic state except for Ta, Nb, and minor for Zr. This implies that the surface composition of HEMG is highly homogeneous compared to that of HEA (Figure 8).[26] This difference can be seen as a function of oxygen concentration in Tables S2 and S3.

The electrochemical measurements were performed in aqueous Ringer's physiological solution. The electrolytes used were NaCl (9 g/L), $CaCl_2$ (0.24 g/L), KCl (0.43 g/L), and $NaHCO_3$ (0.23 g/L). Figure 9a shows that the corrosion analysis started in a stable condition. In addition, it shows that after immersing the samples in a solution for sufficient time, an outstanding, steady state was obtained for HEA compared to HEMG. Figure 9b shows a comparison of the potentiodynamic curves of both amorphous (HEMG) and polycrystalline (HEA) TiZrNbMoTa with the control (Ti without coating). The values obtained from EC-lab software, namely, I_{corr}, I_{pass}, E_{corr}, and corrosion rate (Figure 9), are listed in Table 5. The potentiodynamic curves (Figure 9) and Table 5 indicate that both HEA and HEMG exhibited no significant difference in

https://doi.org/10.1021/acsomega.3c02222
ACS Omega 2023, 8, 28333−28343

Table 6. Elastic (E) and Hardness (H) Elastic and Plastic Deformation (H/E) and (H^3/E^2), Respectively, for Both TiZrNbMoTa HEA and HEMG[a]

sample	E (GPa)	H (GPa)	H/E	H^3/E^2
TiZrNbMoTa (HEA)	139 (±5.9)	10.0 (±0.34)	0.07	0.052
TiZrNbMoTa (HEMG)	186 (±7)	10.3 (±0.17)	0.055	0.032

[a]The modulus and hardness values were obtained from nanoindentation.

corrosion current density (I_{corr}) and corrosion potential (E_{corr}) but showed better I_{corr} and corrosion rate (CR) for an amorphous film, which is well inconsistent with the literature.[26] Nevertheless, both films had well-established passive regions.[26] In particular, the I_{corr} (0.25 μA/cm^2 for HEA and 0.22 μA/cm^2 for HEMG) value was considerably better for the thin films prepared compared with the bulk form of TiZrNbMoTa, which exhibited an I_{corr} of 0.89 μA/cm^2.[29] Furthermore, no pitting potential was observed because of the stable oxide layer.[29]

Nanoindentation analysis was performed with a maximum applied load of 3 mN and a holding time of 3 s. The graph for load vs. penetration depth was plotted. The maximum admissible penetration depth was up to 10% of the film thickness to avoid the substrate effect.[4] Both amorphous and polycrystalline coatings exhibited high hardness and good wear resistance regarding mechanical applications. However, the amorphous coating (HEMG) exhibited higher hardness (10.3 GPa) and modulus (186 GPa) compared to the polycrystalline (HEA) coating, which exhibited a hardness of 10 GPa and modulus of 139 GPa. This higher hardness and modulus for the amorphous coating is considered to be due to the lower crystallite size (Table 2).

Furthermore, the prepared thin films (HEA and HEMG) were subjected to in vitro biocompatibility analysis. A coating was deposited on a CP-Ti substrate, which has been extensively used in medical implants,[25,30,31] to enhance and modify its surface properties as an implant. The amorphous coating exhibited significantly high cell viability for MC3T3-E1 osteoblast cells, as shown in Figure 10. The reason for the high cell viability for HEMG is attributed to the smoother, nonporous, and sufficiently homogeneous surface confirmed by AFM, cross-sectional SEM, and XPS surface analyses. The higher cell proliferation is also due to the higher Ti and Zr contents on the surface (Figure 11).[26]

The high cell viability for HEA and HEMG over CP-Ti can also be attributed to the nontoxic, stable passive layer made of biocompatible elements, namely, Ti, Zr, Nb, Mo, and Ta, which are strongly bonded, thereby avoiding the release of toxic ions. Therefore, HEA and HEMG are also suggested for prospective application to implants (Table 6).[29,32,33]

4. CONCLUSIONS

This research was initiated to evaluate the effect of various thermodynamic parameters and determine the most effective parameters for preparing the crystalline phase of TiZrNbMoTa at RT. A novel system specialized for synthesizing HEAs using a customizable target system was designed and developed. This system is useful in preparing thin films of desired elements. HEMG showed better results regarding high hardness, modulus, corrosion resistance, high elasticity, and plastic deformation. The EDS composition was the same in both types of coatings, i.e., HEMG and HEA. Further, the phase structure was controlled by ΔS_{mix}, ΔH_{mix}, δ, and film thickness. The crystalline phase was obtained with a thickness of 3.3 μm, and the amorphous phase was obtained with a thickness of 833 nm. In short, both alloys have excellent potential for use in biomedical applications. The results revealed that the coating made of HEMG exhibited an outstanding in vitro biological response, which could be modified for further use in biomedical applications. The highly oxidized native layer (Nb_2O_5, Ta_2O_5, TiO_2, ZrO_2, Zr_2O_3 MoO_2, and MoO_3), minor metallic state for HEMG, and higher contents of Ti and Zr make HEAMG increasingly noncytotoxic and bioinert compared to HEA. The findings of this work could contribute to breakthroughs in the field of biomedical implants.

■ ASSOCIATED CONTENT

Supporting Information

The Supporting Information is available free of charge at https://pubs.acs.org/doi/10.1021/acsomega.3c02222.

Various characterization techniques of the thin film, i.e., energy-dispersive spectroscopy (EDS) data from the target; cross-sectional SEM micrographs; enthalpy of mixing for binary elements (ΔH_{mixAB}); EDS data; X-ray photoelectron spectroscopy (XPS) and their corresponding binding energies; and EDS compositions (PDF)

■ AUTHOR INFORMATION

Corresponding Authors

Chul-Kyu Park − *Gachon Pain Center and Department of Physiology, College of Medicine, Gachon University, Incheon 21999, Republic of Korea*; Email: pck0708@gachon.ac.kr

Kwangmin Lee − *School of Materials Science & Engineering, Chonnam National University, Gwangju 61186, Republic of Korea*; Email: kmlee@jnu.ac.kr

Hoonsung Cho − *School of Materials Science & Engineering, Chonnam National University, Gwangju 61186, Republic of Korea*; Email: cho.hoonsung@jnu.ac.kr

Authors

Khurshed Alam − *School of Materials Science & Engineering, Chonnam National University, Gwangju 61186, Republic of Korea; Powder Materials Division, Korea Institute of Materials Science, 51508 Changwon, South Korea*; orcid.org/0000-0001-8115-4711

Woohyung Jang − *Department of Prosthodontics, School of Dentistry, Chonnam National University, Gwangju 61186, Republic of Korea*

Geonwoo Jeong − *School of Materials Science & Engineering, Chonnam National University, Gwangju 61186, Republic of Korea*

Complete contact information is available at: https://pubs.acs.org/10.1021/acsomega.3c02222

Author Contributions

⊥K.A. and W.J. contributed equally to this work.

Notes

The authors declare no competing financial interest.

■ ACKNOWLEDGMENTS

This research was supported by Basic Science Research Program through the National Research Foundation of Korea (NRF) funded by the Ministry of Education (2021R1l1A1A01058691) and by a National Research Foundation of Korea (NRF) grant funded by the Korea Government (MSIT) (No. 2021R1F1A1064062).

■ REFERENCES

(1) Qin, G.; Xue, W.; Fan, C.; Chen, R.; Wang, L.; Su, Y.; Ding, H.; Guo, J. Effect of Co content on phase formation and mechanical properties of (AlCoCrFeNi) 100-xCox high-entropy alloys. *Mater. Sci. Eng., A* **2018**, *710*, 200−205.

(2) Cantor, B.; Chang, I.; Knight, P.; Vincent, A. Microstructural development in equiatomic multicomponent alloys. *Mater. Sci. Eng., A* **2004**, *375*−*377*, 213−218.

(3) Yeh, J. W.; Chen, S. K.; Lin, S. J.; Gan, J. Y.; Chin, T. S.; Shun, T. T.; Tsau, C. H.; Chang, S. Y. Nanostructured high-entropy alloys with multiple principal elements: novel alloy design concepts and outcomes. *Adv. Eng. Mater.* **2004**, *6*, 299−303.

(4) Alvi, S.; Jarzabek, D. M.; Kohan, M. G.; Hedman, D.; Jenczyk, P.; Natile, M. M.; Vomiero, A.; Akhtar, F. Synthesis and Mechanical Characterization of a CuMoTaWV High-Entropy Film by Magnetron Sputtering. *ACS Appl. Mater. Interfaces* **2020**, *12*, 21070−21079.

(5) An, Z.; Jia, H.; Wu, Y.; Rack, P. D.; Patchen, A. D.; Liu, Y.; Ren, Y.; Li, N.; Liaw, P. K. Solid-solution CrCoCuFeNi high-entropy alloy thin films synthesized by sputter deposition. *Mater. Res. Lett.* **2015**, *3*, 203−209.

(6) Guo, H.-X.; Wang, W.-M.; He, C.-Y.; Liu, B.-H.; Yu, D.-M.; Liu, G.; Gao, X.-H. Entropy-Assisted High-Entropy Oxide with a Spinel Structure toward High-Temperature Infrared Radiation Materials. *ACS Appl. Mater. Interfaces* **2022**, *14*, 1950−1960.

(7) Alshataif, Y. A.; Sivasankaran, S.; Al-Mufadi, F. A.; Alaboodi, A. S.; Ammar, H. R. Manufacturing Methods, Microstructural and Mechanical Properties Evolutions of High-Entropy Alloys: A Review. *Met. Mater. Int.* **2019**, *26*, 1099−1133.

(8) Ratner, B. D.; Hoffman, A. S.; Schoen, F. J.; Lemons, J. E.*Biomaterials Science: An Introduction to Materials in Medicine*; San Diego, California, 2004; pp 162−164.

(9) Balla, V. K.; Bose, S.; Davies, N. M.; Bandyopadhyay, A. Tantalum—A bioactive metal for implants. *JOM* **2010**, *62*, 61−64.

(10) Tsaryk, R.; Peters, K.; Barth, S.; Unger, R. E.; Scharnweber, D.; Kirkpatrick, C. J. The role of oxidative stress in pro-inflammatory activation of human endothelial cells on Ti6Al4V alloy. *Biomaterials* **2013**, *34*, 8075−8085.

(11) Castro, D.; Jaeger, P.; Baptista, A. C.; Oliveira, J. P. An Overview of High-Entropy Alloys as Biomaterials. *Metals* **2021**, *11*, No. 648.

(12) Fritze, S.; Koller, C. M.; von Fieandt, L.; Malinovskis, P.; Johansson, K.; Lewin, E.; Mayrhofer, P. H.; Jansson, U. Influence of Deposition Temperature on the Phase Evolution of HfNbTiVZr High-Entropy Thin Films. *Materials* **2019**, *12*, No. 587.

(13) Guo, S.; Liu, C. T. Phase stability in high entropy alloys: Formation of solid-solution phase or amorphous phase. *Prog. Nat. Sci.: Mater. Int.* **2011**, *21*, 433−446.

(14) Guo, S.; Hu, Q.; Ng, C.; Liu, C. T. More than entropy in high-entropy alloys: Forming solid solutions or amorphous phase. *Intermetallics* **2013**, *41*, 96−103.

(15) He, Q.; Yang, Y. On lattice distortion in high entropy alloys. *Front. Mater.* **2018**, *5*, No. 42.

(16) Ye, Y.; Wang, Q.; Lu, J.; Liu, C.; Yang, Y. High-entropy alloy: challenges and prospects. *Mater. Today* **2016**, *19*, 349−362.

(17) Song, H.; Lee, S.; Lee, K. Thermodynamic parameters, microstructure, and electrochemical properties of equiatomic TiMoVWCr and TiMoVNbZr high-entropy alloys prepared by vacuum arc remelting. *Int. J. Refract. Met. Hard Mater.* **2021**, *99*, No. 105595.

(18) Saha, M., A brief discussion on High-entropy alloys vs Compositionally Complex alloys. 2021.

(19) Wu, Y.; Liaw, P. K.; Zhang, Y. Preparation of Bulk TiZrNbMoV and NbTiAlTaV High-Entropy Alloys by Powder Sintering. *Metals* **2021**, *11*, 1748.

(20) Suryanarayana, C.; Norton, M. G. Precise Lattice Parameter Measurements. In *X-Ray Diffraction: A Practical Approach*; Suryanarayana, C.; Norton, M. G., Eds.; Springer US: Boston, MA, 1998; pp 153−166.

(21) Hakan, G.; Mohsen, Z. A novel medium entropy alloy based on iron-manganese-aluminum-nickel: influence of boron addition on phase formation, microstructure, and mechanical properties. *Mater. Res. Express* **2020**, *7*, No. 016516.

(22) Shittu, J.; Pole, M.; Cockerill, I.; Sadeghilaridjani, M.; Reddy, L. V. K.; Manivasagam, G.; Singh, H.; Grewal, H. S.; Arora, H. S.; Mukherjee, S. Biocompatible High Entropy Alloys with Excellent Degradation Resistance in a Simulated Physiological Environment. *ACS Appl. Bio Mater.* **2020**, *3*, 8890−8900.

(23) Mather, R. R. 13 - Surface modification of textiles by plasma treatments. In *Surface Modification of Textiles*; Wei, Q., Ed.; Woodhead Publishing, 2009; pp 296−317.

(24) Pouilleau, J.; Devilliers, D.; Garrido, F.; Durand-Vidal, S.; Mahé, E. Structure and composition of passive titanium oxide films. *Mater. Sci. Eng., B* **1997**, *47*, 235−243.

(25) Cemin, F.; Luís Artico, L.; Piroli, V.; Andrés Yunes, J.; Alejandro Figueroa, C.; Alvarez, F. Superior in vitro biocompatibility in NbTaTiVZr(O) high-entropy metallic glass coatings for biomedical applications. *Appl. Surf. Sci.* **2022**, *596*, No. 153615.

(26) Cemin, F.; Artico, L. L.; Piroli, V.; Yunes, J. A.; Figueroa, C. A.; Alvarez, F. Superior in vitro biocompatibility in NbTaTiVZr (O) high-entropy metallic glass coatings for biomedical applications. *Appl. Surf. Sci.* **2022**, *596*, No. 153615.

(27) Baltrusaitis, J.; Mendoza-Sanchez, B.; Fernandez, V.; Veenstra, R.; Dukstiene, N.; Roberts, A.; Fairley, N. Generalized molybdenum oxide surface chemical state XPS determination via informed amorphous sample model. *Appl. Surf. Sci.* **2015**, *326*, 151−161.

(28) Gondal, M.; Fasasi, T.; Baig, U.; Mekki, A. Effects of Oxidizing Media on the Composition, Morphology and Optical Properties of Colloidal Zirconium Oxide Nanoparticles Synthesized via Pulsed Laser Ablation in Liquid Technique. *J. Nanosci. Nanotechnol.* **2017**, *18*, 4030−4039.

(29) Wang, S.-P.; Xu, J. TiZrNbTaMo high-entropy alloy designed for orthopedic implants: As-cast microstructure and mechanical properties. *Mater. Sci. Eng., C* **2017**, *73*, 80−89.

(30) Rho, K.; Park, C.; Alam, K.; Kim, D.; Ji, M.-K.; Lim, H.-P.; Cho, H. Biological effects of plasma-based graphene oxide deposition on titanium. *J. Nanomater.* **2019**, *2019*, No. 9124989.

(31) Jang, W.; Kim, H.-S.; Alam, K.; Ji, M.-K.; Cho, H.-S.; Lim, H.-P. Direct-deposited graphene oxide on dental implants for antimicrobial activities and osteogenesis. *Int. J. Nanomed.* **2021**, *Volume 16*, 5745−5754.

(32) Yang, W.; Liu, Y.; Pang, S.; Liaw, P. K.; Zhang, T. Bio-corrosion behavior and in vitro biocompatibility of equimolar TiZrHfNbTa high-entropy alloy. *Intermetallics* **2020**, *124*, No. 106845.

(33) Alam, K.; Jo, Y. Y.; Park, C.-K.; Cho, H. Synthesis of graphene oxide using atmospheric plasma for prospective biological applications. *Int. J. Nanomed.* **2020**, *15*, 5813.

https://doi.org/10.1021/acsomega.3c02222
ACS Omega 2023, 8, 28333−28343